

Supplementary Materials for

Outstanding radiation resistance of tungsten-based high-entropy alloys

O. El-Atwani*, N. Li, M. Li, A. Devaraj, J. K. S. Baldwin, M. M. Schneider, D. Sobieraj,
J. S. Wróbel, D. Nguyen-Manh, S. A. Maloy, E. Martinez*

*Corresponding author. Email: oelatwan25@gmail.com (O.E.); enriquem@lanl.gov (E.M.)

Published 1 March 2019, *Sci. Adv.* **5**, eaav2002 (2019)
DOI: 10.1126/sciadv.aav2002

The PDF file includes:

Section S1. HEA morphology and thermal stability

Section S2. Thermal stability

Section S3. Irradiation

Section S4. Mechanical properties

Section S5. Enthalpies of mixing

Section S6. Chemical ordering

Section S7. Dose values

Fig. S1. Alloy structure.

Fig. S2. Bright-field TEM micrographs W-Ta-Cr-V HEA alloy as a function of time during the thermal stability experiment performed in situ with TEM, showing no change in the grain sizes of the nanocrystalline or the ultrafine grains but slight black spots in some grains (precipitation).

Fig. S3. APT analysis of the HEA after annealing at 1050 K.

Fig. S4. Bright-field TEM micrographs as a function of dpa of in situ 1-MeV Kr⁺²-irradiated HEA at 1073 K using a dpa rate of 0.0006 dpa s⁻¹.

Fig. S5. Bright-field TEM micrographs as a function of dpa of in situ 1-MeV Kr⁺²-irradiated HEA at room temperature using a dpa rate of 0.0006 dpa s⁻¹.

Fig. S6. Mechanical response of the HEA.

Fig. S7. Enthalpies of mixing of all binary alloys in the quaternary W-Ta-Cr-V system obtained from DFT and CE calculations.

Fig. S8. Average SRO parameters in the W₃₈Ta₃₆Cr₁₅V₁₁ alloy as a function of temperature.

Fig. S9. Atomic configurations for a W₃₈Ta₃₆Cr₁₅V₁₁ alloy obtained from MC simulations.

Fig. S10. Ion and displacement damage distribution of 1-MeV Kr⁺² and 3-MeV Cu⁺ in the HEA.

Other Supplementary Material for this manuscript includes the following:

(available at advances.sciencemag.org/cgi/content/full/5/3/eaav2002/DC1)

Movie S1 (.avi format). Irradiation of the HEA films at low dose and 1073 K.

Movie S2 (.avi format). Irradiation of the HEA films at high dose and 1073 K.
Movie S3 (.avi format). Irradiation of the HEA films at room temperature.

Section S1. HEA morphology and thermal stability

The morphology and phase details of the as deposited HEA films are shown in fig. S1. As evident in the bright-field TEM micrograph (fig. S1(a)), the films are of bimodal grain size distribution with $\sim 70\%$ of the grains with size in the nanocrystalline regime (≤ 100 nm) and some regions of ultrafine grain sizes (100-500 nm). The inset in fig. S1(a) shows the electron diffraction pattern of the films and demonstrate a single BCC phase with a lattice constant of ~ 3.2 Å. XRD diffraction was performed to confirm that the HEA system was a single phase (fig. S1(b)).

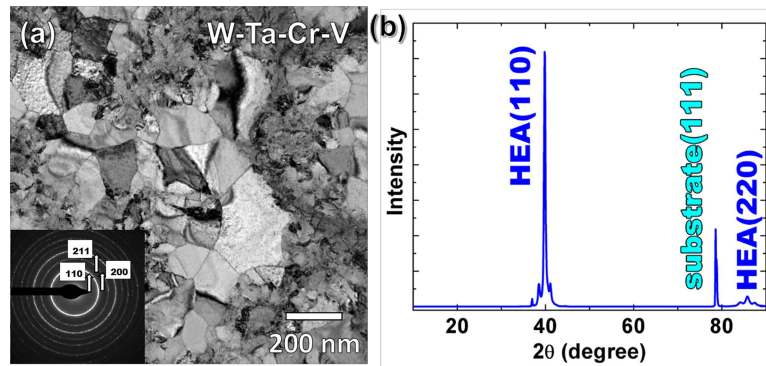


Fig. S1. Alloy structure. (a) Bright-field TEM micrograph of the HEA film showing nanocrystalline (< 100 nm) and ultrafine (100-500 nm) grains (inset shows the electron diffraction pattern and demonstrates one single BCC phase in the alloy). (b) XRD plot of the HEA film showing one single BCC phase in the alloy.

Section S2. Thermal stability

Figure S2 shows the thermal stability of the HEA films as given *in situ* by TEM with temperatures up to 1073 K. Changes in grain sizes were not observed. Film bending due to stresses during the annealing process results in slight variations in the contrast of some grains. Above 1023 K, some grains exhibited black spots (slight segregation of certain elements). Not all grains demonstrated compositional clustering indicating grain variations regarding elemental segregation. Figure S2(h) shows a higher magnification image of these spots. Figure S3 shows the results from APT analysis for an annealed sample at 1050 K. APT shows clear compositional layering visible in both the ion maps and 2D composition maps in fig. S3.

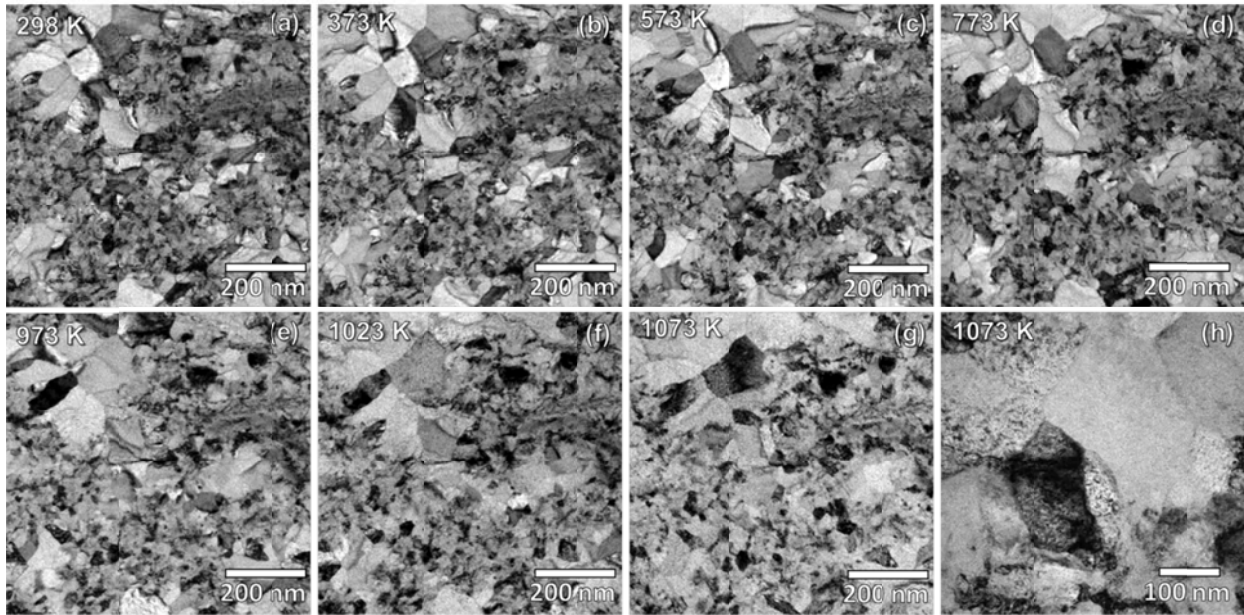


Fig. S2. Bright-field TEM micrographs W-Ta-Cr-V HEA alloy as a function of time during the thermal stability experiment performed *in situ* with TEM, showing no change in the grain sizes of the nanocrystalline or the ultrafine grains but slight black spots in some grains (precipitation).

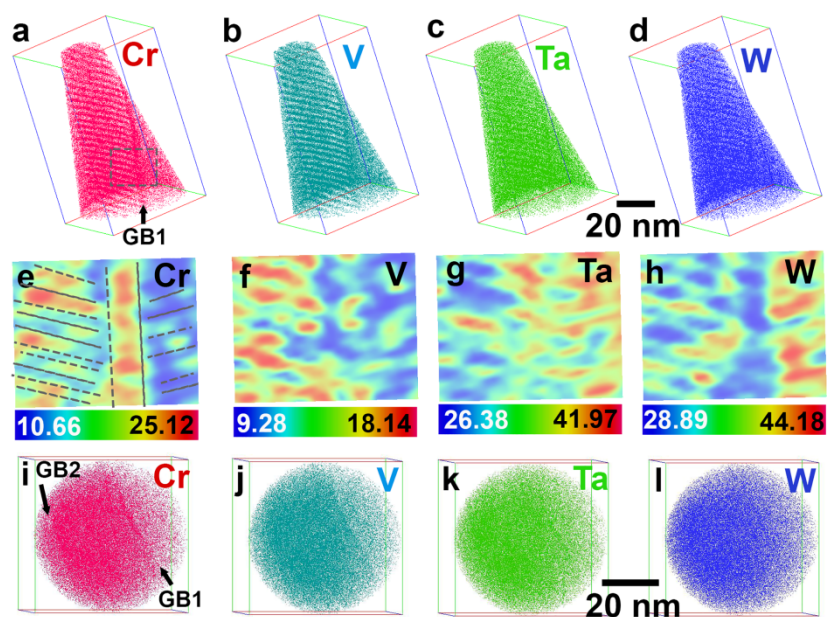


Fig. S3. APT analysis of the HEA after annealing at 1050 K. (a)-(d) 3D distribution of Cr, V, Ta and W in the 1050 K HEA. (e)-(h) 2D compositional maps of Cr, V, Ta and W using a 25x1x20nm slice. (i)-(l) top-down view showing the location of two distinct grain boundaries as well as the corresponding elemental segregation.

Section S3. Irradiation

The morphology of the samples before and during irradiation at 1073 K is shown in fig. S4.

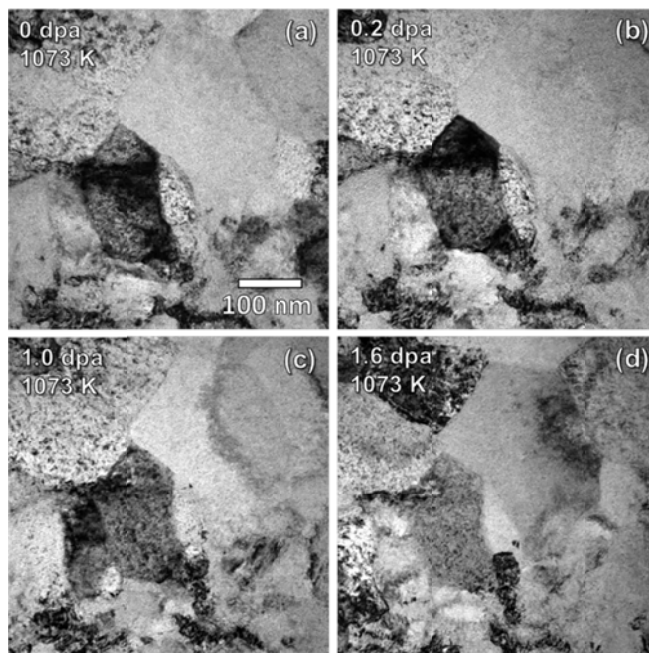


Fig. S4. Bright-field TEM micrographs as a function of dpa of in situ 1-MeV Kr^{+2} -irradiated HEA at 1073 K using a dpa rate of $0.0006 \text{ dpa s}^{-1}$. (a) pre-irradiation, (b) 0.2 dpa, (c) 1.0 dpa and (d) 1.6 dpa. Images show enhanced precipitation (black spot formation) in some grains. All images have the same scale bar.

While the morphology of the samples before and during irradiation at 298 K is shown in fig. S5.

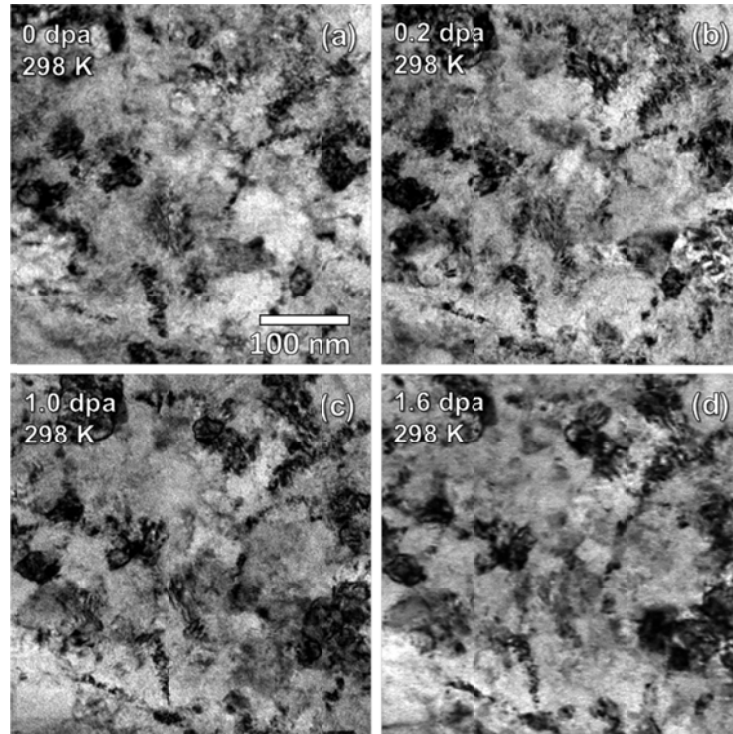


Fig. S5. Bright-field TEM micrographs as a function of dpa of in situ 1-MeV Kr⁺²-irradiated HEA at room temperature using a dpa rate of 0.0006 dpa s⁻¹. (a) pre-irradiation, (b) 0.2 dpa, (c) 1.0 dpa and (d) 1.6 dpa. Images show not much precipitation (black spots formation). All images have the same scale bar.

Section S4. Mechanical properties

The mechanical properties of this material were investigated on thicker films ($\sim 3\mu\text{m}$) before irradiation, after annealing and after *ex situ* irradiation with 3 MeV Cu⁺ to ~ 17 peak dpa (with a dpa rate of 0.02 dpa.s⁻¹) via nanoDMA. Figure S6 shows representative load versus displacement curves and hardness versus displacement curves for the samples. The shift of the loading curves to the left (fig. S6(a)) indicate an increase in hardness which is confirmed by the hardness versus displacement curves (fig. S6(b)). The sample annealing results in a hardness increase which is slightly enhanced by irradiation (8 dpa) (fig. S6(c)).

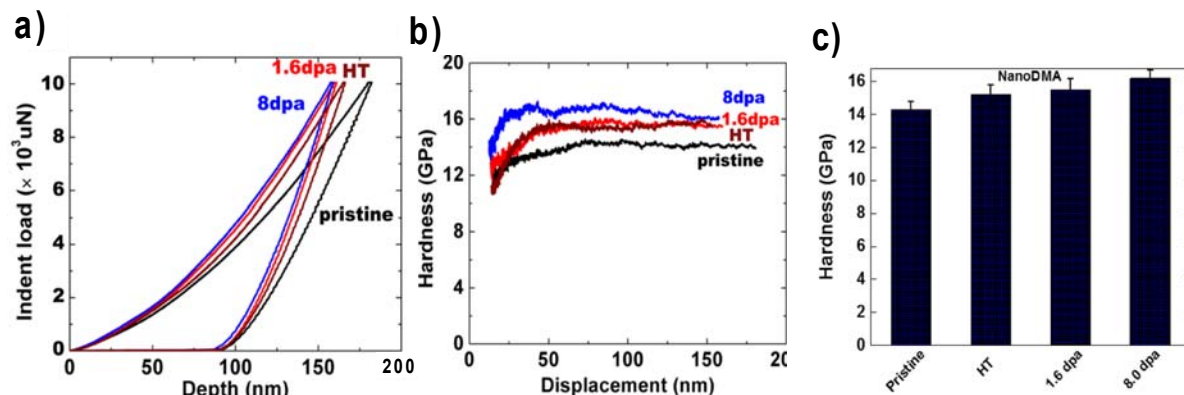


Fig. S6. Mechanical response of the HEA. Representative (a) load-displacement curves and (b) hardness vs displacement curves for the pristine, annealed samples to 1073 K (HT), 1.6 dpa and 8 dpa irradiated samples. Shift of loading curves to the left indicates slight hardening, which is confirmed from the hardness vs displacement curves. (c) Nano-hardness (using nanoDMA) values of the pristine, annealed (HT), 1.6 dpa and 8 dpa irradiated HEA samples.

Section S5. Enthalpies of mixing

Enthalpy of mixing results for all binary alloys in the quaternary system W-Ta-Cr-V as obtained with both density-functional theory and cluster expansion methodologies.

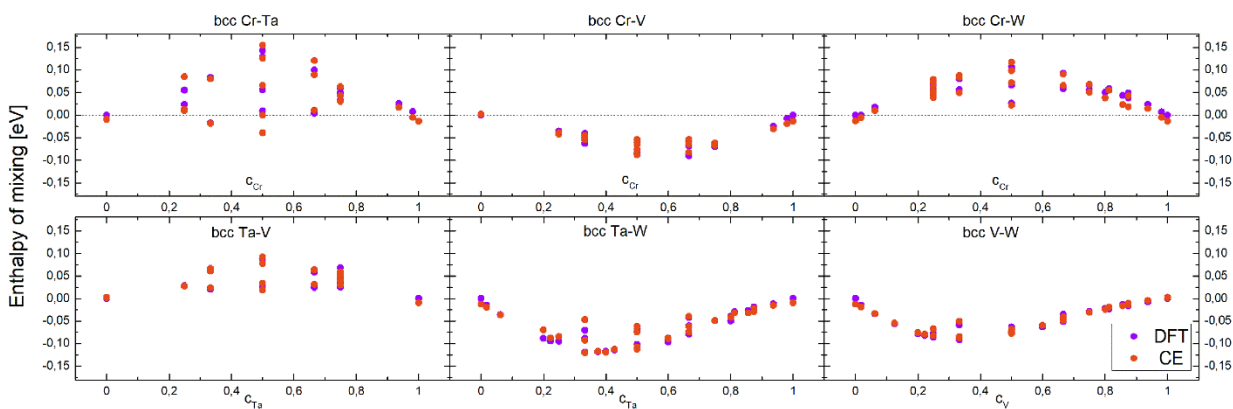


Fig. S7. Enthalpies of mixing of all binary alloys in the quaternary W-Ta-Cr-V system obtained from DFT and CE calculations.

Section S6. Chemical ordering

Chemical ordering in alloys can be investigated analysing the Warren-Cowley short-range order (SRO) parameters^{51,52}. For atoms i and j being in the n -th nearest neighbor shell in either binary or multicomponent alloys these parameters can be defined as

$$\alpha_n^{ij} = 1 - \frac{y_n^{ij}}{c_i c_j} = 1 - \frac{P_n^{i-j}}{c_j}$$

where c_i and c_j are the concentrations of i 's and j 's atoms, and $P_n^{i-j} = \frac{y_n^{ij}}{c_i}$ is the conditional

probability of finding atom i in the n th coordination sphere of atom j . Positive α_n^{ij} characterize a segregated system, whereas negative values indicate ordering. The pair correlation function y_n^{ij} can be mathematically obtained from the inversion of the average cluster function $\langle \Gamma_{\omega'}(\vec{\sigma}) \rangle$ for the pairs⁴⁴. Figure S8 shows the SRO dependence for these alloys as a function of temperature.

The SRO is defined as the average of the α_n^{ij} values in the system. The figure shows a negative chemical SRO for the two pairs between V-Cr and W-Ta and positive for the other four pairs W-Cr, W-V, Ta-V and Ta-Cr at temperatures lower than 1400K. There is a strong chemical bonding between Cr and V whereas it becomes less pronounced for chemical order between W and Ta. This finding implies a strong segregation tendency of Cr and V.

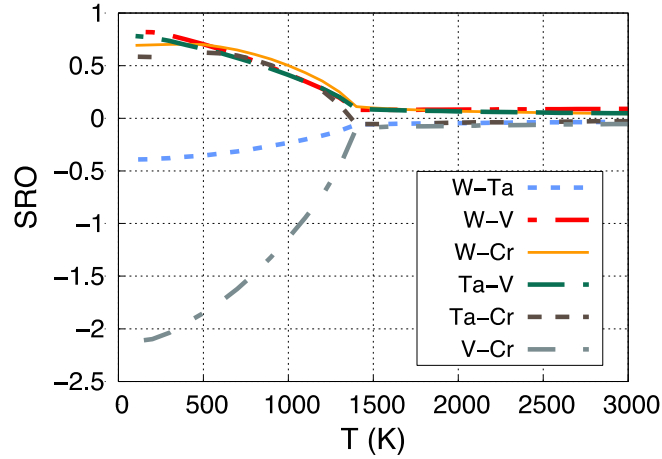


Fig. S8. Average SRO parameters in the $W_{38}Ta_{36}Cr_{15}V_{11}$ alloy as a function of temperature.

Figure S9 shows the atomic configurations of $W_{38}Ta_{36}Cr_{15}V_{11}$ obtained from canonical Monte Carlo (CMC) simulations within a 30x30x30 BCC cell at $T=300K$ and $T=1000K$.

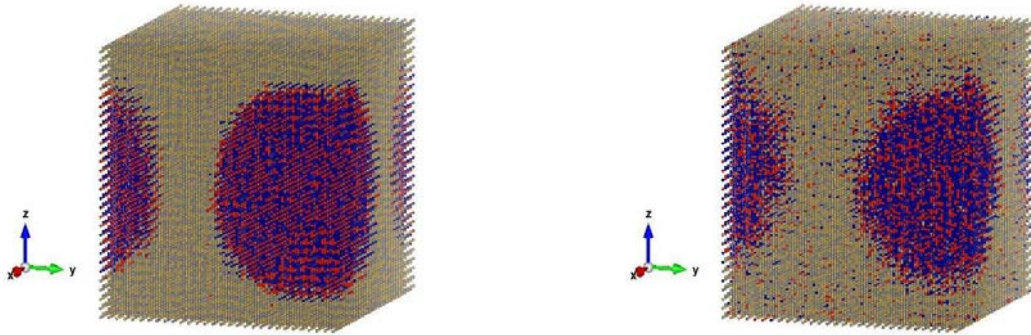


Fig. S9. Atomic configurations for a $W_{38}Ta_{36}Cr_{15}V_{11}$ alloy obtained from MC simulations. (left) $T=300K$ and (right) $T=1000K$.

Section S7. Dose values

Dose values depending on the sample depth are shown in fig. S10 and S11 as obtained using the Kinchin-Pease model in the Stopping Range of Ions in Matter (SRIM) Monte Carlo computer code (version 2013) with a displacement threshold energy of 40 eV.

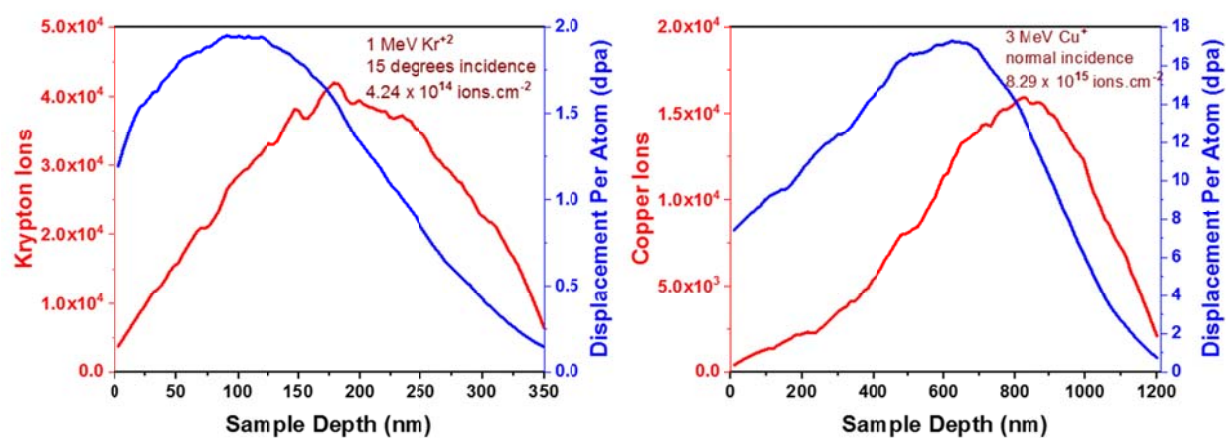


Fig. S10. Ion and displacement damage distribution of 1-MeV Kr^{+2} and 3-MeV Cu^+ in the HEA.